ADVANCES IN ATMOSPHERIC SCIENCES, VOL. 39, MAY 2022, 763–781

• **Original Paper** •

# Initiation and Evolution of Long-Lived Eastward-Propagating Mesoscale Convective Systems over the Second-Step Terrain along Yangtze-Huaihe River Valley※

Yuanchun ZHANG*[1], Jianhua SUN[1,2,3], Ruyi YANG[4], and Ruoyun MA[1,3]

[1]*Key Laboratory of Cloud-Precipitation Physics and Severe Storms (LACS), Institute of Atmospheric Physics, Chinese Academy of Sciences, Beijing* 100029, *China*

[2]*Southern Marine Science and Engineering Guangdong Laboratory (Zhuhai), Zhuhai* 519080, *China*

[3]*University of the Chinese Academy of Sciences, Beijing* 100049, *China*

[4]*Public Meteorological Service Center, China Meteorological Administration, Beijing* 100044, *China*

(Received 17 August 2021; revised 9 December 2021; accepted 5 January 2022)

ABSTRACT

Based on the previous statistical analysis of mesoscale convective systems (MCSs) over the second-step terrain along Yangtze-Huaihe River Valley, eight representative long-lived eastward-propagating MCSs are selected for model-based sensitivity testing to investigate the initiation and evolution of these types of MCSs as well as their impact on downstream areas. We subject each MCS to a semi-idealized (CNTL) simulation and a sensitivity (NOLH) simulation that neglects condensational heating in the formation region. The CNTL experiment reveals convection forms in the region downstream of a shortwave trough typified by persistent southwesterly winds in the low-to midtroposphere. Upon merging with other convective systems, moist convection develops into an MCS, which propagates eastward under the influence of mid-tropospheric westerlies, and moves out of the second-step terrain. The MCS then merges with pre-existing local convection over the plains; the merged convection reinforces the cyclonic wind perturbation into a mesoscale vortex at 850 hPa. While this vortex moves eastward to regions with local vortex at 850 hPa, another vortex at 925 hPa is also intensified. Finally, the vortices at 850 and 925 hPa merge together and develop into a mesoscale convective vortex (MCV). In contrast, MCSs fail to form and move eastward in the NOLH experiment. In the absence of eastward-propagating MCSs, moist convection and mesoscale vortices still appear in the plains, but the vortex strength and precipitation intensity are significantly weakened. It is suggested the eastward-propagating MCSs over the second-step terrain significantly impact the development and enhancement of moist convection and vortices in the downstream areas.

**Key words:** mesoscale convective systems, second-step terrain, mesoscale convective vortex, numerical sensitivity simulation

**Citation:** Zhang, Y. C., J. H. Sun, R. Y. Yang, and R. Y. Ma, 2022: Initiation and evolution of long-lived eastward-propagating mesoscale convective systems over the second-step terrain along Yangtze-Huaihe River Valley. *Adv. Atmos. Sci.*, **39**(5), 763−781, https://doi.org/10.1007/s00376-022-1303-3.

**Article Highlights:**

- Eastward-propagating MCSs from second-step terrain merge with downstream convection and reinforce perturbations into a mesoscale vortex.
- Low-level vortices merge into a MCV over the Yangtze-Huaihe River Valley as the mesoscale vortex moves eastward to local vortex regions.
- These eastward-propagating MCSs significantly impact the development and enhancement of convection and vortices in the downstreams.

## 1. Introduction

Mesoscale convective systems (MCSs) are well-known significant weather systems that produce hazardous weather, such as heavy rain, lightning, and hail (Maddox, 1980; Tollerud and Collander, 1993; Zheng et al., 2013).

※ This paper is a contribution to the special issue on Predictability, Data Assimilation and Dynamics of High Impact Weather —In Memory of Dr. Fuqing ZHANG.

* Corresponding author: Yuanchun ZHANG
Email: zhyc@mail.iap.ac.cn

With improvements in satellite remote sensing and radar detection, many experts explored the spatial and temporal distribution of MCSs (Maddox, 1980; Augustine and Howard, 1991; Laing and Fritsch, 1997). Following Maddox (1980), numerous studies have evaluated the statistical features of MCSs by applying size and duration criteria of the cold cloud shields based on infrared (IR) satellite images in various regions (Augustine and Caracena, 1994; Laing and Fritsch, 1997; Anderson and Arritt, 1998; Mathon and Laurent, 2001; Jirak et al., 2003; Rafati et al., 2017; Zheng et al., 2008; Yang et al., 2015, Yang et al., 2020). Because of the complex terrain distribution in China, there are regional differences in the spatial and temporal features of MCSs in China (Zheng et al., 2008; Qi and Zheng, 2009). Most previous studies of MCSs in China have focused on the Tibetan Plateau (TP) and Yangtze-Huaihe River Valley (YHRV). Mesoscale convective systems (MCSs) over the TP show clear temporal variation with a peak frequency of occurrence in the afternoon. Over the Sichuan Basin, MCSs mostly occur during the nighttime, and convection over the plains can also initiate during the afternoon and early morning (Jiang and Fan, 2002; Zheng et al., 2008; Bai et al., 2011; Fu et al., 2013; Hu et al., 2016).

However, few studies have paid attention to MCSs on the second-step terrain in China. The second-step terrain usually refers to the high mountain ranges from the Da Hinggan Mountains over northeast China (including the Yanshan Mountains, the Taihangshan Mountains, the Loess Plateau, and the Mongolian Plateau over north China and the Qinling Mountains over central China) to the Yunnan-Guizhou Plateau over southwest China (partly shown in Fig. 1a). Some studies have found that severe convective systems appear over the YHRV to the east of the second-step terrain (Meng et al., 2013; Zheng et al., 2013; Zheng and Sun, 2016). Previous simulation studies show that these convective systems can be traced back to convective systems over the second-step terrain (He and Zhang, 2010; Sun and Zhang, 2012; Zhang and Sun, 2017, Zhang et al., 2018). Many studies found that the initiation mechanisms of MCSs are different when the underlying surface conditions are different (Velasco and Fritsch, 1987; Trier and Parsons, 1993; Laing and Fritsch, 1997; Zipser et al., 2006; Zheng et al., 2008; Qi and Zheng, 2009, Rasmussen and Houze, 2011; Luo et al., 2014; He et al., 2018; Zhuo et al., 2012 ). Some case studies found that latent heating over the second-step terrain enhances the intensity, longevity, and eastward movement of mesoscale vortices over the eastern plains (Fu et al., 2017). In addition, the combination of the mountain-plain solenoid (MPS), due to the heating difference between the second-step terrain and its eastern plains, and the enhanced nocturnal low-level jet (LLJ) favored convection initiation east of the second-step terrain (Zhang et al., 2014, 2018).

The above mentioned previous findings are concluded from case studies. Therefore, it is crucial to explore and summarize the common mechanisms responsible for the initiation and development of MCSs over the second-step terrain. A recent statistical study identified and tracked MCSs around the second-step terrain along the middle reaches of the YHRV (the region is shown in the solid brown box in Fig. 1b) and classified these MCSs into eastward-propagating and quasi-stationary types (Yang et al., 2019, 2020). It is found that eastward-propagating MCSs, which originate from the second-step terrain, enhance the precipitation in downstream regions. Based on these studies, eight long-lived eastward-propagating MCSs over the second-step terrain will be selected objectively in the present study to explore their initiation and detail their impact on downstream regions. Section 2 introduces the objective method used to select the typical MCS cases. Section 3 elaborates on the specific model design of the semi-idealized simulation. The initiation and evolution characteristics of this type of long-lived eastward-propagating MCSs are analyzed in section 4. The results of the sensitivity experiment are discussed in section 5. Finally, conclusions and discussion are presented in section 6.

## 2. Case selection

A total of 316 eastward-propagating MCSs that form over the second-step terrain are divided into four categories according to their key features (such as their initiation, trajectories, and termination, Yang et al., 2019). One of the four categories for MCSs (i.e., a set of 55 MCSs) consists of those that had the longest lifetime and made the largest contribution to warm-season heavy rainfall (the tracks of these 55 MCSs are shown in Fig. 1b) in downstream regions of second-step terrain. To explore the common mechanisms of initiation and development of these long-lived MCSs and their impact on downstream regions, the correlation coefficients related to the geopotential height of the 500 hPa surface in the key region for these 55 MCSs are calculated to select the MCS cases which initiate and develop under similar synoptic circulations. The key region at 500 hPa is determined as the region covering 100°–120°E, 26.5°–36.5°N (the solid brown rectangle in Fig. 1b). The correlation coefficients for these 55 long-lived eastward-propagating MCSs at their formation time in the key region are calculated using the following formula:

$$\mathrm{cor} = \frac{\sum_{i=1}^{n}\left(h'_{i,j}-\overline{h'_j}\right)\left(h'_{i,k}-\overline{h'_k}\right)}{\sqrt{\sum_{i=1}^{n}\left(h'_{i,j}-\overline{h'_j}\right)^2\sum_{i=1}^{n}\left(h'_{i,k}-\overline{h'_k}\right)^2}},$$

where $h'_{i,j} = h_{i,j} - \bar{h}_{i,j}$ and $h'_{i,j}$ is the perturbation geopotential height for case $j$ at grid point $i$, $\underline{j}$ is the geopotential height for case $j$ at grid point $i$, and $\bar{h}_{i,j}$ is the climatological average geopotential height for case $j$ at grid point $i$ during May–August from 2000 to 2016 (except 2015). The geopotential height, $h'_{i,k}$ is the same as $h'_{i,j}$, but for case $k$. The perturbation geopotential heights for cases $j$ and $k$ averaged over the key region are indicated by $\overline{h'_j}$ and $\overline{h'_k}$, respectively. The number of grid points in the key region is represented

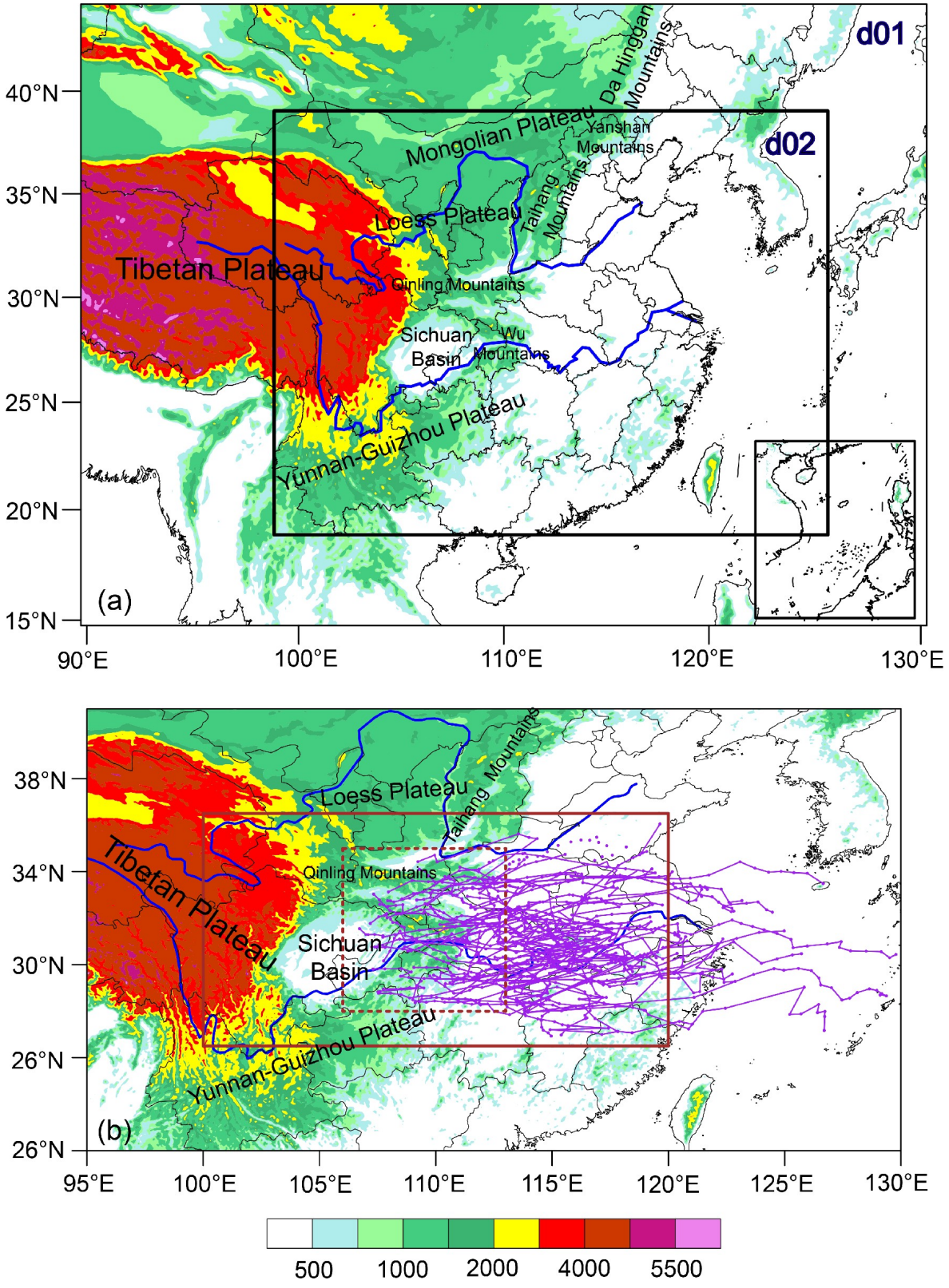


**Fig. 1.** (a) Distribution of terrain elevation higher than 500 m (units: m, color shading), d01 and d02 stand for the domains of the simulations in the text. (b) Distribution of terrain height higher than 500 m (units: m, color shading), the solid brown rectangle represents the key region used for correlation coefficient calculation, and the brown dashed rectangle outlines the region in which MCSs form (formation region) and the saturation latent heating is turned off. The purple trajectories are the tracks of 55 MCSs, which initiate over the second-step terrain and propagate eastward to the downstream regions.

by $n$, and cor represents the correlation coefficient of perturbation geopotential height between each two cases in the key region.

Based on calculations using the above formula, we identified eight representative MCSs among the long-lived eastward-propagating 55 MCSs, for which the correlation coefficient between any two exceeds 0.6. In addition, all eight MCSs have lifetimes longer than 15 h, with precipitation falling over regions east of 115°E (Table 1). At 500 hPa (Fig. 2), case 7 is influenced by a cold vortex in the south and airflow around the periphery of the Western Pacific subtropical high (WPSH), whereas the remaining cases are characterized by a westerly trough located east of the Tibetan Plateau (TP) and a strengthened WPSH with its ridge extending westward to 110°E. Mesoscale convective systems (MCSs) form in the region of southwesterly winds associated with the trough and WPSH, where warm air advection and positive vorticity advection provide favorable environmental conditions for convective initiation. Although the synoptic weather patterns at 500 hPa are generally the same among the eight MCSs, the low-level weather patterns differ. An examination of the 850 hPa weather pattern for the eight MCSs suggests that all MCSs form in the mid-eastern mountainous region of the second-step terrain along YHRV with only a slight difference in the exact locations (figures not shown). The precipitation distribution associated with the eight MCSs extends from the Qinling Mountains to downstream areas. The tracks of the MCSs with the largest spatial influence span the middle and lower reaches of YHRV and the East China Sea. Among the eight MCSs, cases 3 and 4 produced the most accumulated precipitation (over 30 mm), while cases 7 and 8 are associated with less precipitation (Fig. 3). The rain bands associated with the eight MCSs generally cover the region east of the second-step terrain to the middle and lower reaches of YHRV; therefore, they are representative of the MCSs over this region and are appropriate to use for further simulation and mechanism studies.

## 3. Experiment configuration

Due to the limited spatial and temporal resolution of conventional observational data, numerical simulations are used in the present study to investigate the influence of long-lived eastward-propagating MCSs on precipitation over the second-step terrain along YHRV in the downstream region. The primary goal of the current study is to examine the impact of the second-step terrain on the initiation of MCSs. Some previous studies have employed semi-idealized numerical simulations to reveal the common impact of terrain on the MCSs and the associated mechanism of diurnal variation (Trier et al., 2010; Sun and Zhang, 2012; Chen et al., 2016). Specifically, semi-idealized numerical simulations are carried out using the Weather Research and Forecasting model (WRF, V3.8; Skamarock and Klemp, 2008). The initial and boundary conditions are averaged from the selected eight MCSs provided by the Climate Forecast System Reanalysis (CFSR) dataset from the National Centers for Environmental Prediction (NCEP) with a horizontal grid spacing of 0.5° × 0.5° at 6-hour time intervals. Composite initial and boundary conditions are obtained based on the following scheme. The formation time of the MCS is defined as Tn(0), with n representing the sequence number for eight real cases. The formation time is defined herein as the first time when the contiguous cold cloud shield of the MCS (TBB ⩽ 221 K) reaches an area of at least 5000 km$^2$. Since the temporal resolution of the reanalysis data is 6 h, the field at 6 hours before the formation time is denoted as Tn(−6), and that for 6 hours after the formation time is denoted as Tn(6), and so on. The simulation covers the period from 12 hours before to 24 hours after the formation time, which gives a simulation period of 36 h, so the initial conditions are given by the average field of the eight MCSs cases at Tn(−12), and the boundary conditions are obtained from the composite fields of eight MCSs at Tn(−6), Tn(0), Tn(6), Tn(12), Tn(18), and Tn(24), respectively. The simulation starts at 12 hours before the formation time of the eight MCSs (defined as $t$ = 00 h), which is 0200 Local Standard Time (LST, LST = UTC + 8; LST is used hereafter).

The model domain is illustrated in Fig. 1a. Two one-way nested domains with a 9 km and 3 km horizontal grid spacing are used, which yields 530 lon. × 390 lat. and 1039 lon. × 796 lat. grids, respectively, in the two domains. A total of 50 sigma layers are set in the vertical with the model top at 50 hPa. For both the inner and outer domains, the WRF single-moment 6-class microphysics scheme (WSM6; Hong and Lim, 2006), the Rapid Radiative Transfer Model

**Table 1**. Time and location of the formation and termination of eight MCSs.

| Case number | Formation time | Termination time | Formation longitude (°E) | Formation latitude (°N) | Formation height (m) |
|---|---|---|---|---|---|
| 1 | 2000062720 | 2000062822 | 107.19 | 31.77 | 545.05 |
| 2 | 2001062808 | 2001062904 | 112.46 | 33.75 | 639.05 |
| 3 | 2002062207 | 2002062307 | 112.86 | 32.30 | 173.69 |
| 4 | 2016062217 | 2016062320 | 108.54 | 32.83 | 766.44 |
| 5 | 2003070110 | 2003070203 | 107.96 | 33.13 | 597.88 |
| 6 | 2006062108 | 2006062205 | 111.34 | 31.06 | 612.49 |
| 7 | 2010081314 | 2010081405 | 107.93 | 32.75 | 1207.59 |
| 8 | 2012070810 | 2012070901 | 109.54 | 32.62 | 849.81 |

Notes: time is denoted in yyyymmddhh, i.e., 2000062620 means 2000 UTC 27 June 2000.

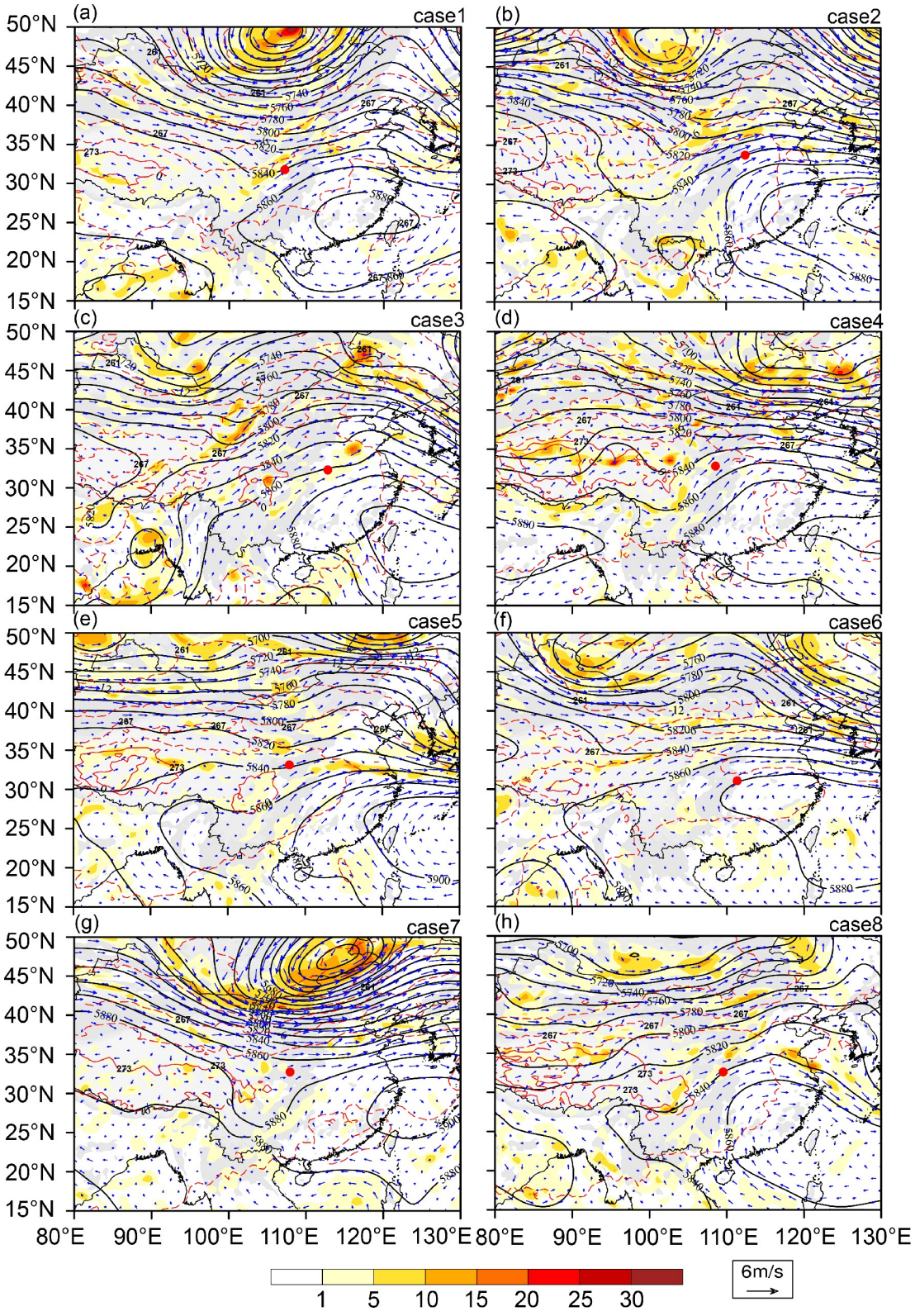


**Fig. 2.** The synoptic weather pattern at 500 hPa for the eight eastward-propagating MCS cases at their formation time: geopotential height (solid black contours, units: gpm). temperature (red dashed contours, units: K), wind (blue arrow, units: m $s^{-1}$), and relative vorticity (color shading, units: $10^{-6}$ $s^{-1}$). The red dots represent the formation locations of MCSs. Grey shading represents terrain elevations > 500 m. (a) Case 1 at 0500 LST 28 June 2000; (b) case 2 at 1700 LST 28 June 2001; (c) case 3 at 1400 LST 22 June 2002; (d) case 4 at 0200 LST 23 June 2016; (e) case 5 at 1700 LST 01 July 2003; (f) case 6 at 1700 LST 21 June 2006; (g) case 7 at 2300 LST 13 August 2010; (h) case 8 at 1700 LST 8 July 2012.

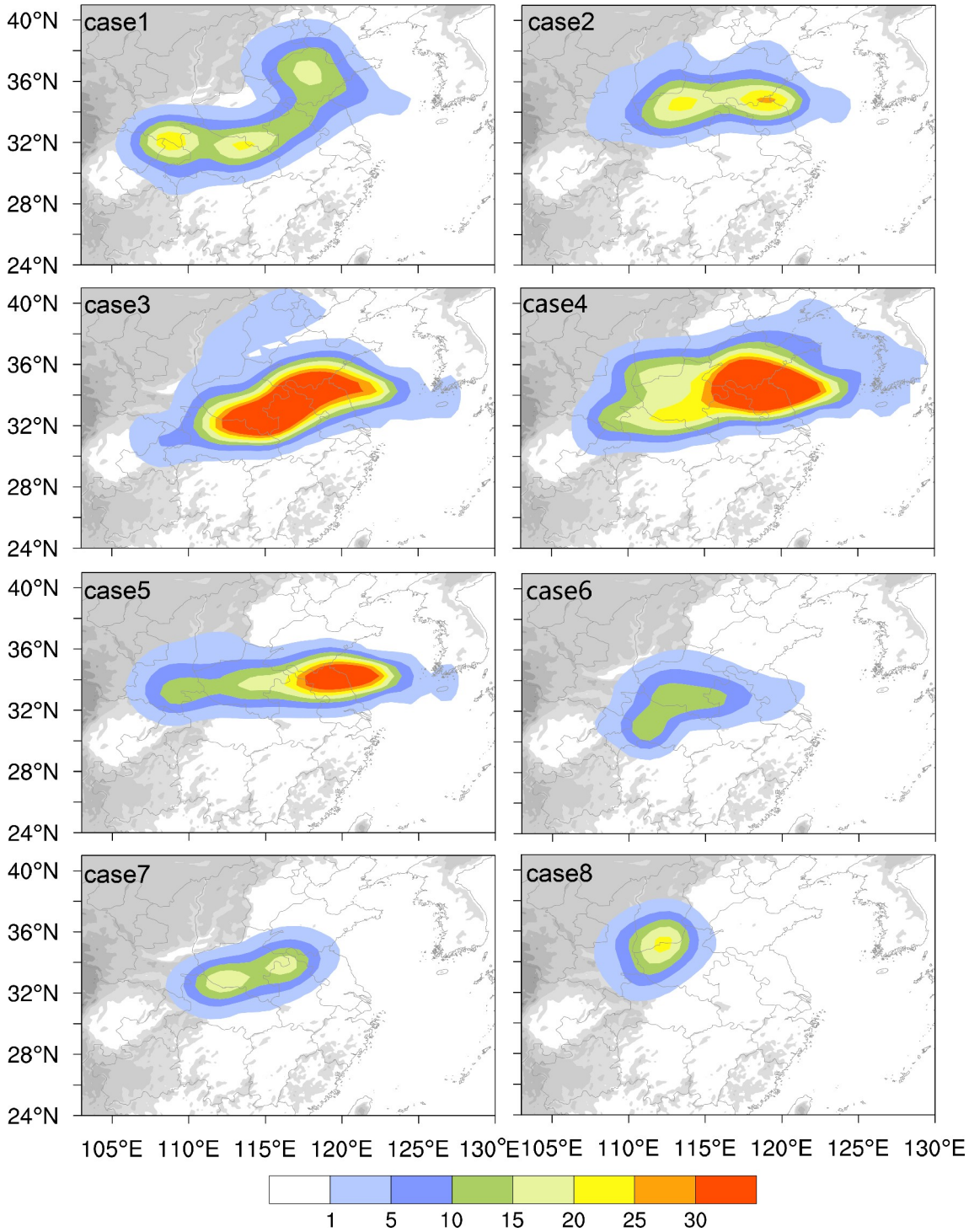


**Fig. 3.** Distribution of accumulated precipitation (color shading, units: mm) during the lifetimes of the eight MCSs. Grey shading represents terrain elevations > 500 m.

(RRTM) longwave radiation scheme (Mlawer et al., 1997), the Dudhia shortwave radiation scheme (Dudhia, 1989), the Noah land surface model scheme (Chen and Dudhia, 2001), the Yonsei University (YSU) planetary boundary layer scheme (Hong et al., 2006) are used. The Kain-Fritsch cumulus parameterization (Kain, 2004) is applied to the outer domain. The above setting is referred to as the CNTL experiment.

Latent heating is a key factor for the organization, development, and maintenance of moist convection. It is thought to be difficult for convection to organize into MCSs if inadequate latent heating release is present after convection initiation. Therefore, a sensitivity experiment with the diabatic heating in the formation region (106°–113°E, 28°–35°N)

turned off (NOLH) is performed to study the impact of terrain on long-lived eastward-propagating MCSs and precipitation over downstream areas.

## 4. Results from the CNTL simulation

### 4.1. *Verification of CNTL results*

The composite circulation of the eight MCSs at 500 hPa at 0200 LST shows that the shortwave trough is located at the eastern edge of the Tibetan Plateau and Sichuan Basin. At the same time, the WPSH covers the region south of YHRV and South China. Southwesterly winds on the periphery of WPSH favor the eastward propagation of MCSs to the middle and lower reaches of YHRV (figures not shown). In the lower levels of the troposphere (i.e., 925 hPa), cyclonic wind shear is maintained over the lee side of the second-step terrain. The associated cyclonic curvature in the wind field continually intensifies, which finally gives rise to the formation of a mesoscale vortex over the boundaries between Henan, Anhui, and Shandong Provinces by 0200 LST the following day. The vortex intensifies and propagates eastward to downstream regions (Figs. 4a, c, e, g). The synoptic circulation pattern at 500 hPa in the CNTL simulation is similar to that of the composite results from eight real cases in reanalysis data. Still, the simulated WPSH in lower latitudes is slightly stronger than that of the reanalysis data, thereby exerting control over areas further west (the simulated 5880 gpm isohypse extends west of 110°E). In addition, the simulated trough in the westerlies to the east of the TP is stronger (figure not shown). The simulated flow at 925 hPa reproduces vortex formation over the eastern edge of the second-step terrain, its development, and eastward propagation. The formation location of the vortex in the simulation agrees well with that from composite results, but the simulated vortex is stronger (Figs. 4b, d, f, h). Figure 5 compares long-lived eastward-propagating trajectories between the eight simulated MCSs and eight real MCS cases. The simulated contiguous cold cloud of the MCS reaches 5000 km$^2$ at 1530 LST, which is delayed by about 1.5 h compared to the composite results (the MCS forms at 1400 LST). In general, the simulation reproduces the average locations of the eight MCSs during their formation, eastward propagation, and dissipation stages (Fig. 5a). The simulated MCS initiates at the eastern edge of the second-step terrain (boundaries between Shaanxi and Hubei Provinces), about 1° further north of the average initiation location of the real cases. After formation, the MCS propagates eastward out of the second-step terrain and influences the southern and central regions of Henan Province, northern areas of Anhui Province, and the YHRV before finally decaying to the east into the sea. The simulated accumulated rainfall distribution from 12 hours before until 12 hours after the MCS formation is basically consistent with that from the eight real MCSs, except that the simulated precipitation maxima are slightly greater in the simulation compared to the real cases (Fig. 5b).

The above comparison between the CNTL and composite results from real cases clearly indicates that the CNTL simulation reproduces the eastward-propagating trajectories, rainbelt coverage, and background synoptic circulation relatively well during MCS evolution. Therefore, the initiation and evolution of long-lived, eastward-propagating MCSs over the second-step terrain along the YHRV are explored based on the simulation results. Additionally, sensitivity experiments are designed to further analyze the latent heating effects on downstream mesoscale systems.

### 4.2. *Formation and evolution of long-lived eastward-propagating MCS*

Based on the simulation results, the formation and evolution of the MCS are characterized by four stages. Namely, the MCS formation stage (1330–1530 LST), propagation stage over the second-step terrain (1500–1900 LST), mesoscale convective vortex (MCV) formation stage (1900–2330 LST), maintenance stage (2330–0900 LST), and the dissipation stage (0830–1400 LST).

#### 4.2.1. *MCS formation stage (1330–1530 LST)*

The 850 hPa convergence between northwesterly winds to the north of the Qingling Mountains and southeasterly winds to the southeast of the Qingling Mountains enhances the vertical motion and cloud-top heights. Convection with cloud-top TBB colder than 221 K (C1; Fig. 6a) first appears over Qingling Mountains in the southeastern areas of Shanxi Province (109.5°E, 33.3°N) at 1330 LST, and the corresponding rainfall intensity is more than 20 mm h$^{-1}$ (Fig. 6a). Meanwhile, the intensified cyclonic circulation over the eastern edge of the second-step terrain (~112°E) leads to the continuous southward advancement of northeasterly winds along the periphery of the circulation, which results in the formation of a convergence region at 1430 LST (Fig. 6b). The northwesterly and southeasterly winds associated with this convergence region trigger a new area of convection to the north of C1 (Fig. 6b; hereafter C2, 110°E, 33.75°N). The new area of convection, C2, gradually intensifies after initiation and merges with C1 about one hour later, leading to the formation of a mesoscale convective system (hereafter MCS1) with a cold cloud shield coverage more extensive than 5000 km$^2$ (Fig. 6c; the MCS criteria in Yang et al., 2020). The rainfall rate associated with MCS1 reached 50 mm h$^{-1}$.

#### 4.2.2. *Propagation stage over the second-step terrain (1530–1900 LST)*

After formation, MCS1 intensifies and propagates eastward over the second-step terrain. In the meantime, a convergence region between the northeasterly and southeasterly winds is located to the east of MCS1 (Fig. 6c). When MCS1 moves into the convergence region, it merges with preexisting isolated convection therein and further intensifies (Fig. 6d). Accordingly, several precipitation centers appear with maximum rainfall intensities reaching 100 mm h$^{-1}$ (Fig. 6d). At 1700 LST (Fig. 7a), while MCS1 propagates eastward on

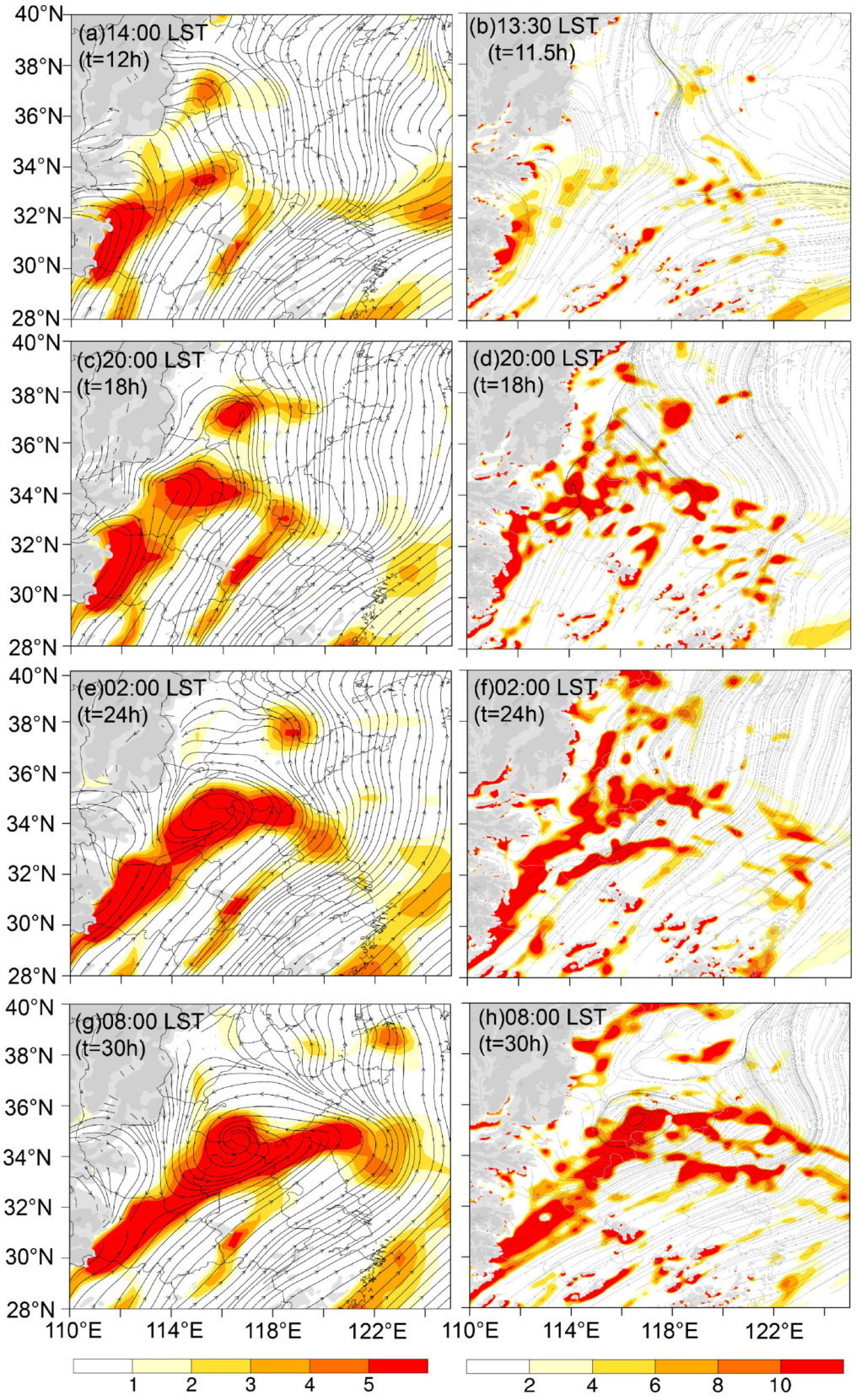


**Fig. 4.** Left column: composite relative vorticity (color shading, units: $10^{-5}$ $s^{-1}$) and flow field at 925 hPa of the eight MCSs using CFSR reanalysis data at (a) 1400 LST, (c) 2000 LST, (e) 0200 LST, and (g) 0800 LST, respectively. Right column: simulated relative vorticity (color shading, units: $10^{-5}$ $s^{-1}$) and flow field (right) at 925 hPa at (b) 1330 LST, (d) 2000 LST, (f) 0200 LST, and (h) 0800 LST. Grey shading represents terrain elevations >500 m.

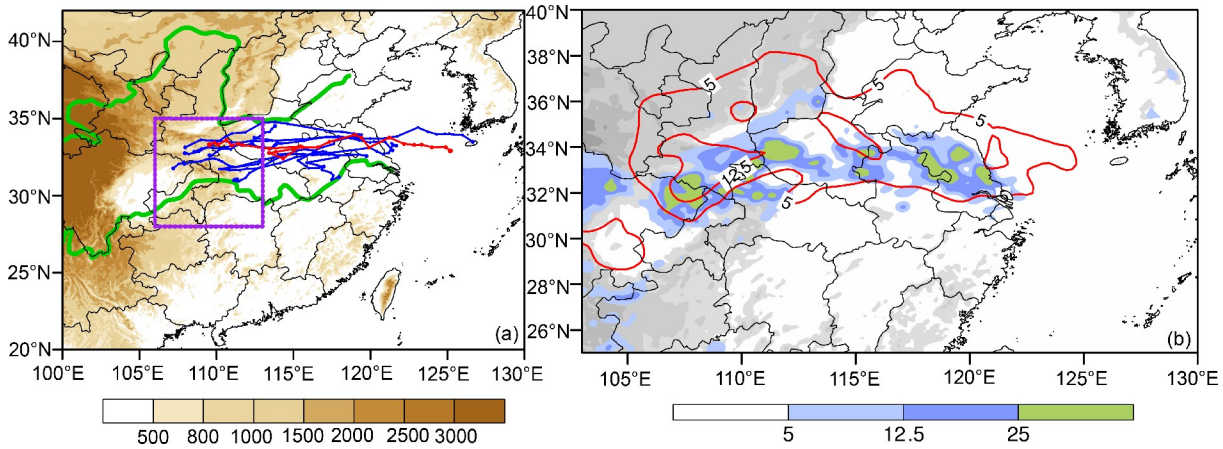


**Fig. 5.** (a) The real propagation trajectories (solid blue lines) of the eight MCSs and the simulated path of the MCS in CNTL simulation (solid red line). Dots represent MCS locations at each time. Brown shading represents terrain elevations > 500 m. Purple box covers the MCS formation regions. (b) Precipitation amounts from 6 h before and 6 h after the formation of MCS averaged over the eight MCSs (red contours, units: mm) and precipitation amount in CNTL simulation (color shading, units: mm). Grey shading represents terrain elevations > 500 m.

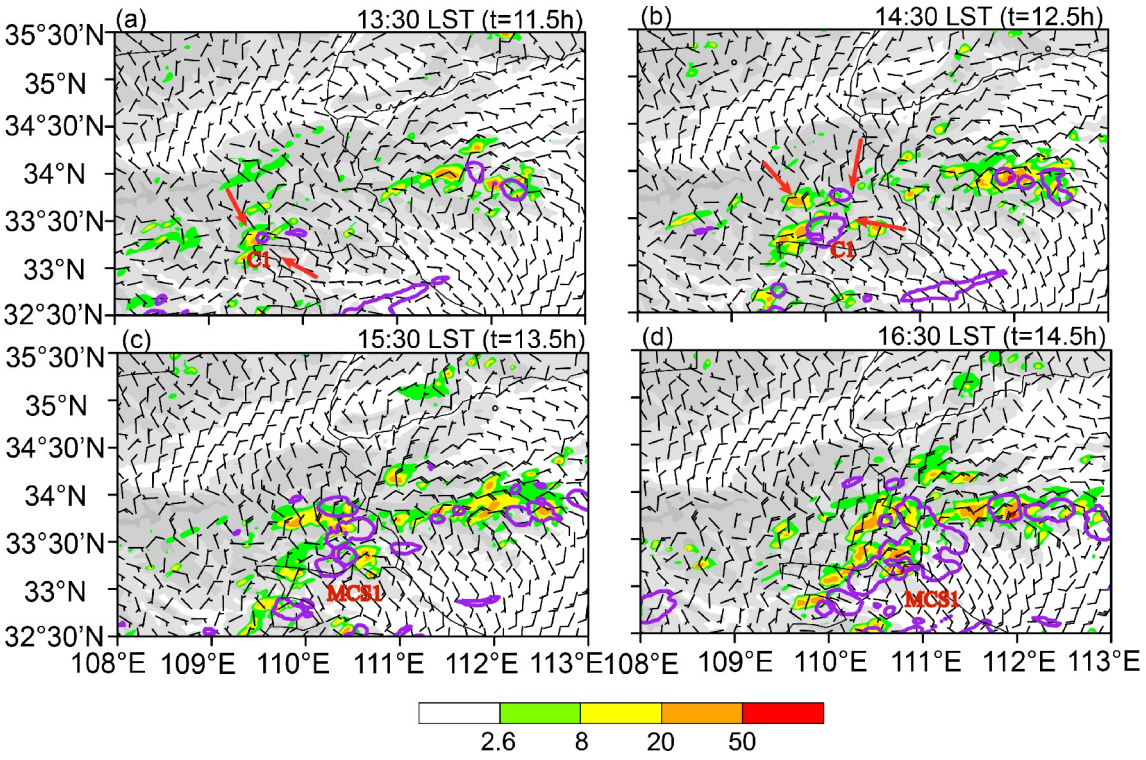


**Fig. 6.** The CNTL results: wind field (wind barb, 4 m $s^{-1}$; speeds with > 8 m $s^{-1}$ are indicated in blue) at 850 hPa, hourly precipitation (color shading, units: mm $h^{-1}$), and boundary of TBB = 221 K in CNTL simulation (purple lines). Grey shading represents terrain elevations > 500 m.

the eastern edge of the second-step terrain, the corresponding wind convergence intensified. The convergence at the northern end of the southwesterly LLJ intensifies and promotes the development of MCS1 at 1900 LST (Fig. 7c).

#### 4.2.3. *MCV formation stage (1900–2300 LST)*

After 1900 LST, the intensified wind perturbation at 850 hPa gradually develops into mesoscale vortices. The initial system, MCS1, moves out of the second-step terrain and merges with local convection in downstream regions at 2000 LST (the merged convection is referred to as MCS hereafter). Meanwhile, because of upward motion appearing at ~1.5 km (figures not shown), wind convergence appears over the plains at 850 hPa (114.4°E, 34.5°N), located to the northeast of the MCS. With the enhancement of upward motion after 2000 LST, the wind convergence develops into a cyclonic vortex (Fig. 7e; V1). The strong wind convergence (113.5°E, 34°N) at 925 hPa first appears at ~2030

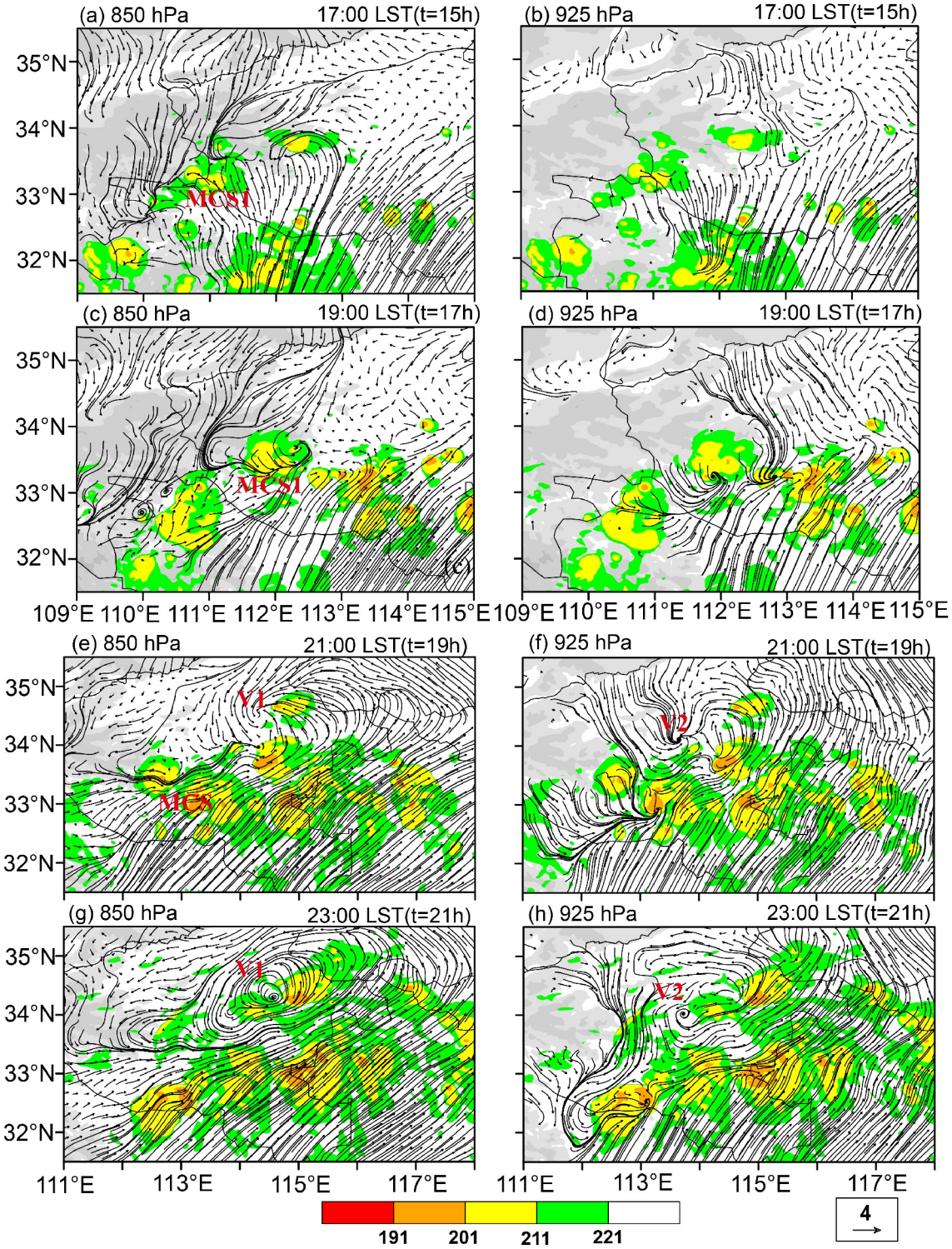


**Fig. 7.** CNTL results: wind field (units: m $s^{-1}$) at 850 hPa (left column) and 925 hPa (right column), TBB (shading, units: K). The grey shading represents the terrain elevations > 500 m.

LST, 30 minutes later than its appearance at 850 hPa. The convergence gradually evolves into a new mesoscale vortex (V2) after 2130 LST (Figs. 7f–h).

After the MCS and its associated vortex propagate eastward out of the second-step terrain and move into the V1 region, the merged V1 intensifies into a mature mesoscale vortex (Fig. 7g). With the enhancement of V1, the strong upward motion extends both upward and downward (figures not shown). The vortex center of V2 at 925 hPa shifts below the V1 center at 2230 LST (Fig. 7h). Subsequently, V2 at 925 hPa combines with the merged V1 at 850 hPa. Finally, the mature MCV forms at lower levels (below 700 hPa)

after 2330 LST.

#### 4.2.4. *Maintenance stage (2300–0900 LST) and dissipation stage (0900–1400 LST)*

The mature MCV structure below 700 hPa is maintained over the YHRV until 0900 LST. However, the MCS accelerates eastward and decays during this MCV maintenance stage. Consistent with the enhanced cyclonic circulation, the precipitation related to the MCV significantly increases before reaching a maximum at 0700 LST (figures not shown), which causes heavy rainfall over the middle reaches of the Yangtze River. The MCV begins to dissipate after 0900 LST; however, cyclonic wind shear is maintained to the east of the mesoscale vortex. The MCV gradually changes its shape into a zonally-oriented elliptical structure. Moreover, the MCV begins to dissipate along with a weakened daytime LLJ, and the related precipitation consequently decreases (figure not shown).

The above analysis divides the evolution period of the MCS and its related MCV into five stages. 1) The MCS formation stage (1330–1530 LST) starts with convection (C1) triggered by the convergence between northwesterly and southeasterly wind at 850 hPa over Qingling Mountains. After propagating eastward and merging with local convection over the mountains, C1 develops into MCS1. 2) The MCS1 moves eastward with its related wind convergence during the propagation stage over the second-step terrain (1530–1900 LST). 3) The MCV formation stage (1900 to 2300 LST) occurs as MCS1 propagates eastward out of the eastern edge of the second-step terrain and merges with preexisting convective systems over the plains, then the merged MCS and its corresponding wind perturbation intensifies at 1930 LST. Meanwhile, the locally triggered vortex (V1) at 850 hPa and V2 at 925 hPa appear over the plains northeast of the MCS after 2230 LST. The 850 hPa vortex (V1) intensifies after the MCS-related vortex moves into the region of V1. The enhanced upward motion of V1 promotes the eastward displacement of the vortex center of V2 at 925 hPa. The combined effects of V1 and V2 initiate the formation of a mature MCV structure (below 700 hPa) over the YHRV. 4) The MCV is maintained and causes heavy rainfall over the middle reaches of the Yangtze River during 2300~0900 LST before dissipating between 0900 and 1400 LST.

### 4.3. *Environmental conditions at convection initiation*

The above analysis demonstrates that the eastward-propagating MCS influences the vortex and precipitation over the downstream regions. However, the above analysis focuses on the stage when the MCS has attained a relatively strong intensity (i.e., after the TBB falls below 221 K). This section will discuss and compare the environmental conditions prior to and after convection initiation. Based on the simulated composite radar reflectivity, a single cell (SC1) with reflectivity larger than 10 dB*Z* appears over the Qinling Mountains (109.27°E, 33.28°N) at 0930 LST (Fig. 8a). Twenty minutes later, the reflectivity increases to the criterion of convection initiation (35 dB*Z*, May and Ballinger, 2007; Zhang et al., 2016). When the convection over upstream regions propagates eastward, SC1 strengthens through its merger with the upstream convection. The cloud-top height of SC1 increases and its TBB decreases. While the TBB above the maximum reflectivity is below 221 K at 1330 LST (Fig. 8e), the convection develops into C1 (Fig. 6a). The environmental conditions before and after SC1 initiation and the initiation mechanism will be further explored in the following.

Favorable thermal and moisture conditions contribute to convection initiation. At 500 hPa, a westerly propagating trough appears east of TP three hours before SC1 initiation (0730 LST) and is maintained. The 5880 gpm isohypse extends westward to 110°E and controls the regions south of 30°N. Convection initiates under southwesterly winds ahead of the trough and on the northwestern periphery of WPSH (Fig. 9b). After convection initiation, the steering winds gradually turn westerly, which favors the eastward propagation of convection. The strong southwesterly wind west of the WPSH transports abundant water vapor and warm airflow into the initiation regions near 700 hPa (Figs. 9c, f), which causes the relative humidity to exceed 90%, high equivalent potential temperature, and strong instability. At lower levels (~850 hPa), the southwesterly wind rotates cyclonically over the lee side of the second-step terrain, transporting abundant warm and moist flow (Fig. 9e). The wind shear between southeasterly and southwesterly wind over the eastern edge of the second-step terrain (about 109.3°E, 33°N) provides favorable dynamic conditions for convection initiation. Temperatures increase to south of the convection initiation location while temperatures decrease to the north of the convection initiation location. The convection tends to initiate over the regions with the highest temperature gradient (Fig. 9f). After convection initiation, the downstream temperature gradient is maintained; cooler temperatures over the northern regions continue to extend eastward, and the temperature over southern regions also increases. Six hours after convection initiation, the temperature gradient in the convection region is still large.

Figure 10 shows the soundings before and after convection initiation at the center of SC1 (109.27°E, 33.27°N). The air is close to saturation, and the convective available potential energy (CAPE) reaches 901 J kg$^{-1}$ at 0920 LST (Fig. 10a). Ten minutes later, the upward motion at low levels overcomes the convective inhibition (CIN), and the ascending air saturates upon reaching the lifting condensation level (LCL) near 830 hPa. The wind veers from low to middle levels consistent with warm advection in this layer. In addition to promoting ascent, the warm advection associated with the southerly wind component promotes atmospheric instability. With the upward extension of the saturation layer, the moist layer deepens, and the CAPE increases to 1080 J kg$^{-1}$ (Fig. 10b). The strong upward motion initiates SC1 at 1020 LST. After convection initiation and the

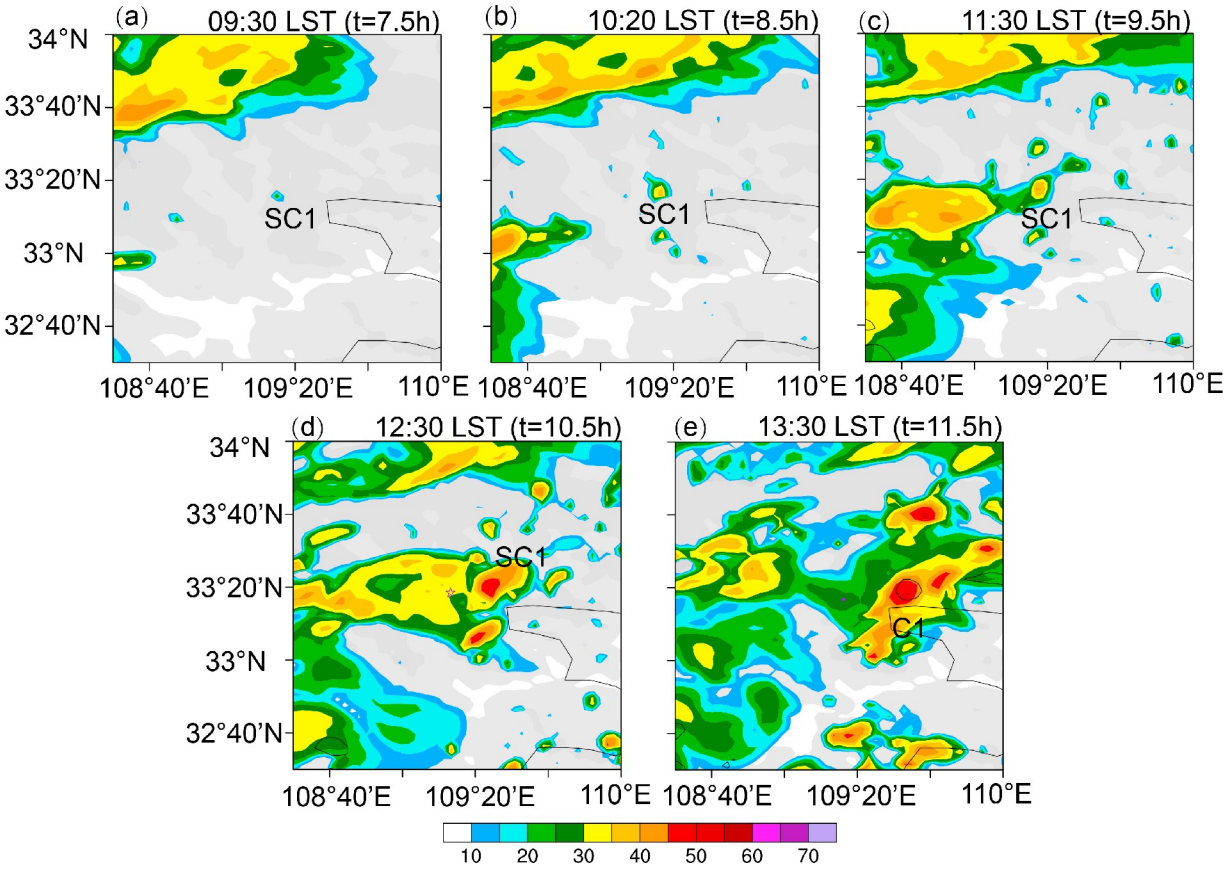


**Fig. 8.** Radar composite reflectivity (shading, units: dBZ ) in CNTL from the 7.5 to 11.5 simulation hours. SC1 symbolizes a single-cell and C1 stands for the convective complex. The grey shading represents terrain elevations > 500 m.

associated release of instability, the CAPE decreases to 332 J kg$^{-1}$ (figure not shown). The equivalent potential temperature increases at 0920 LST (1 h before SC1 initiation), causing the enhancement of the equivalent potential temperature gradient. The maximum gradient appears at SC1 initiation time, 1020 LST (Fig. 10c). After 0940 LST, the condensation and associated latent heat release promotes the strong upward motion under a strong CAPE condition (Fig. 10e). The cloud water mixing ratio rises sharply and extends to upper levels. When the cloud water mixing ratio maximum is lifted to about 650 hPa (figure not shown), the convection initiates at 1020 LST. The vertical cross-section of horizontal wind shear shows that southeasterly wind is maintained at 850 hPa before 0920 LST, then the wind gradually turns to easterly and changes to northeasterly at 0950 LST. Meanwhile, the wind field at 800 hPa turns from southerly to southeasterly. The southwesterly wind is maintained above 750 hPa. The wind speed gradually increases from 750 to 600 hPa before SC1 initiation yet decreases across this layer after SC1 initiation. The above analysis found that the wind veers with height, confirming that warm advection is present in the initiation region. The wind shear increases at middle and lower levels before SC1 initiation, conducive to convective development. After initiation, the enhanced wind shear at middle and upper levels favors the development and organization of convection (Coniglio et al., 2006; Chen et al., 2015).

## 5. Sensitivity experiment results

Based on the CNTL simulation, we chose to perform a sensitivity experiment by turning off the latent heating related to condensation. The experiment is designed to explore the impact of condensational heat release on eastward-propagating MCSs and convection and precipitation in downstream regions. The brown dashed box in Fig.1 illustrates the regions in which the latent heat of condensation is turned off in a way such that the condensational heating and evaporative cooling in the CNTL setting are substituted by the only evaporative cooling in the NOLH experiment (Figs. 11a, b).

The accumulated precipitation from MCS1 formation (1530 LST) until the end time of NOLH simulation of the two simulations is compared in Figs. 12a, b. In the CNTL run, accumulated precipitation greater than 100 mm occurred along a northeast-southwest axis. The associated precipitation maxima was mainly located over the southern regions of Henan Province and northern regions of Jiangsu Province. After turning off the latent heating in the NOLH experiment, the precipitation west of 114°E decreases sharply, and the rainfall over the eastern regions still maintains an east-west orientation. Still, the precipitation max-

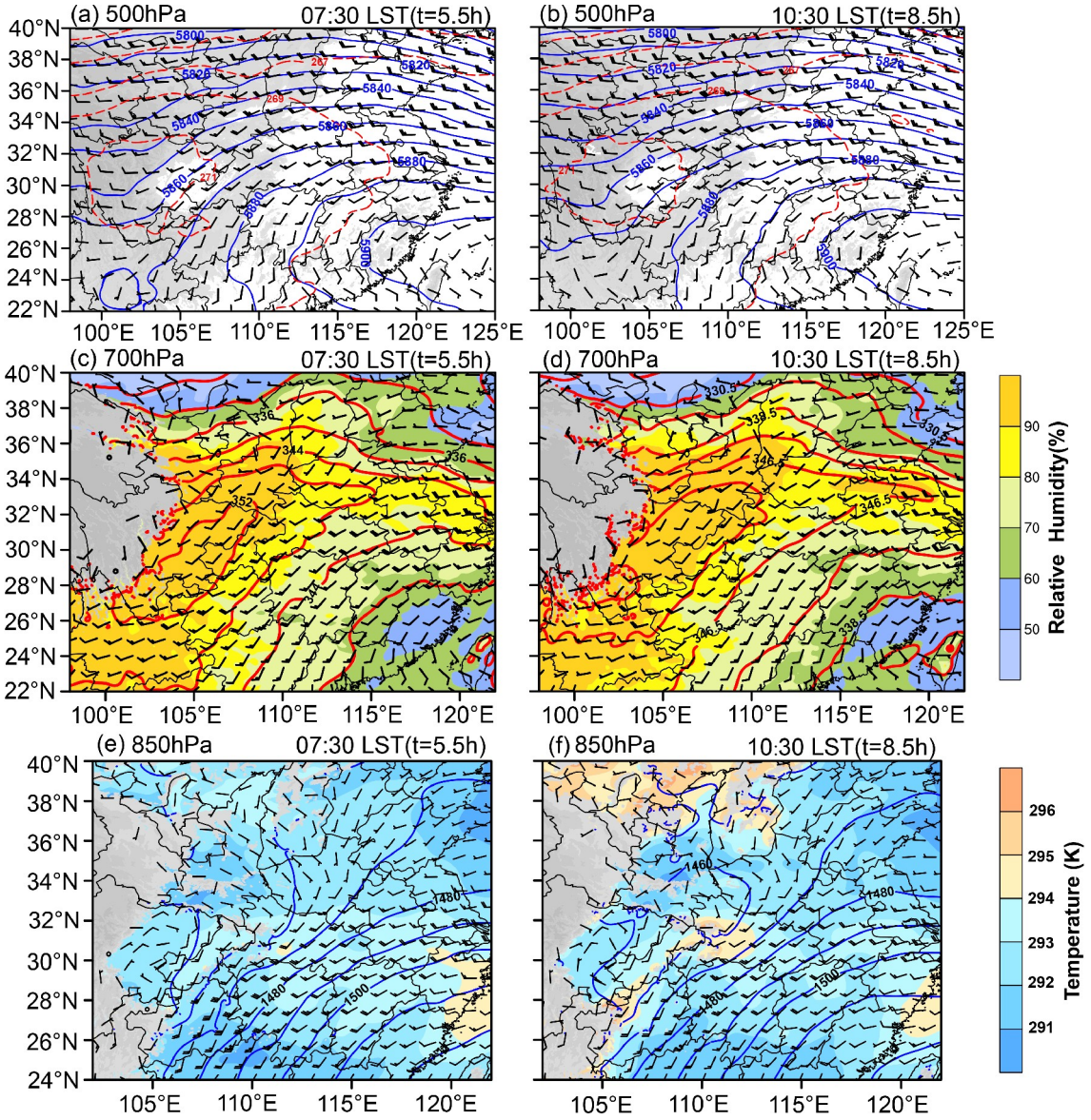


**Fig. 9.** The CNTL results at 0730 LST (left column) and 1030 LST (right column). Panels (a) and (b) are the wind field (wind barb, 5 m $s^{-1}$), geopotential height (solid blue lines, units: gpm), and temperature (red dashed lines, units: K) at 500 hPa. The grey shading represents terrain elevations > 500 m. Panels (c) and (d) show the wind field (wind barb, 5 m $s^{-1}$), equivalent potential temperature (solid red line, units: K), and relative humidity (shading, units: %) at 700 hPa. The grey shading represents terrain elevations > 3000 m. Panels (e) and (f) show the wind field (wind barb, units: 5 m $s^{-1}$), geopotential height (solid blue lines, units: gpm), and temperature (shading, units: K) at 850 hPa. The grey shading represents terrain elevations > 1500 m.

ima maintains itself over the boundaries between Shandong and Jiangsu Provinces.

When the latent heating is turned off over the formation region in the NOLH experiment, the appearance of the first radar reflectivity is delayed, and the reflectivity intensity is weaker. The convection which forms in southern regions of Shanxi Province weakens, and the merged convection does not develop into new MCS1 (figure not shown). Therefore, an MCS is not triggered over the second-step terrain and obviously cannot go on to influence the downstream regions. This result can be used to infer the effects of MCS1 on the weather of downstream regions.

In the CNTL simulation, the MCV over downstream regions maintains itself at lower levels (850 and 925 hPa) at 2000 LST. While the latent heating is turned off in NOLH, the vortex at lower levels still forms at 2000 LST. To compare the vortex intensity in the two simulations, a key region, centered on the vortex with a 300 km × 300 km horizontal extent, is chosen for analysis. The average relative vorticity is calculated within the key region for the period from the formation to maturity of the vortex (Figs. 12c–f). Without the impact of an eastward-propagating MCS, the vor-

tex intensity in NOLH is much weaker than that in CNTL, especially during the first half-period of MCV duration (2000–0130 LST). Moreover, the average vorticity difference between the two simulations in the key region at 925

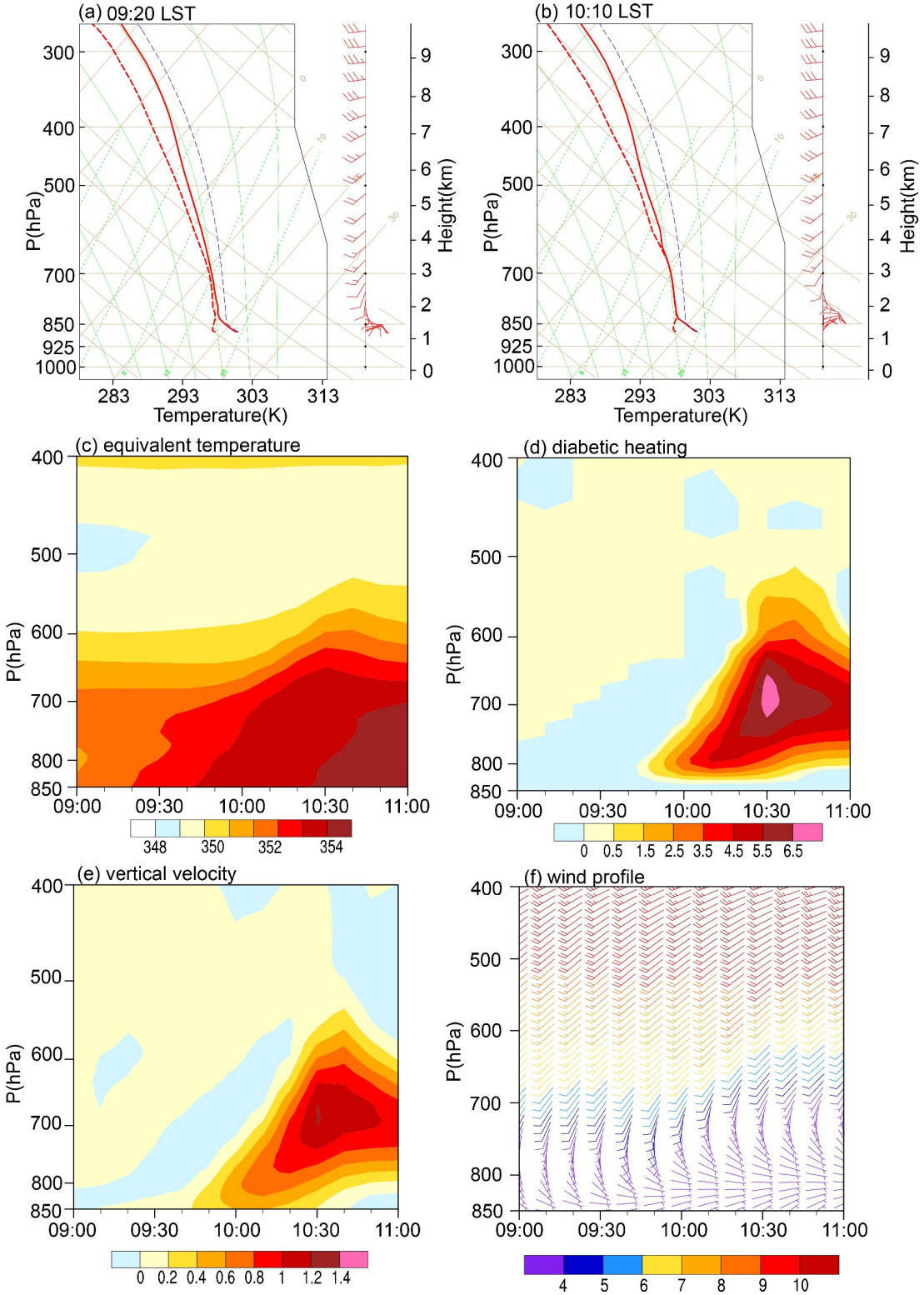


**Fig. 10.** Soundings at the SC1 location in CNTL before initiation, temperature profile (red line), dew point temperature profile (red dashed line), and stratification curve (blue dashed line). Panel (a) is at 0920 LST and (b) 1010 LST. The physical parameters of evolution at SC1 initiation location with time are shown in (c)–(e). Panel (c) is the equivalent temperature (units: K), (d) is diabatic heating (units: $10^{-3}$ K $s^{-1}$), (e) is the vertical velocity (units: m $s^{-1}$), and (f) is horizontal wind field (wind barb, 5 m $s^{-1}$, colors represent wind speeds).

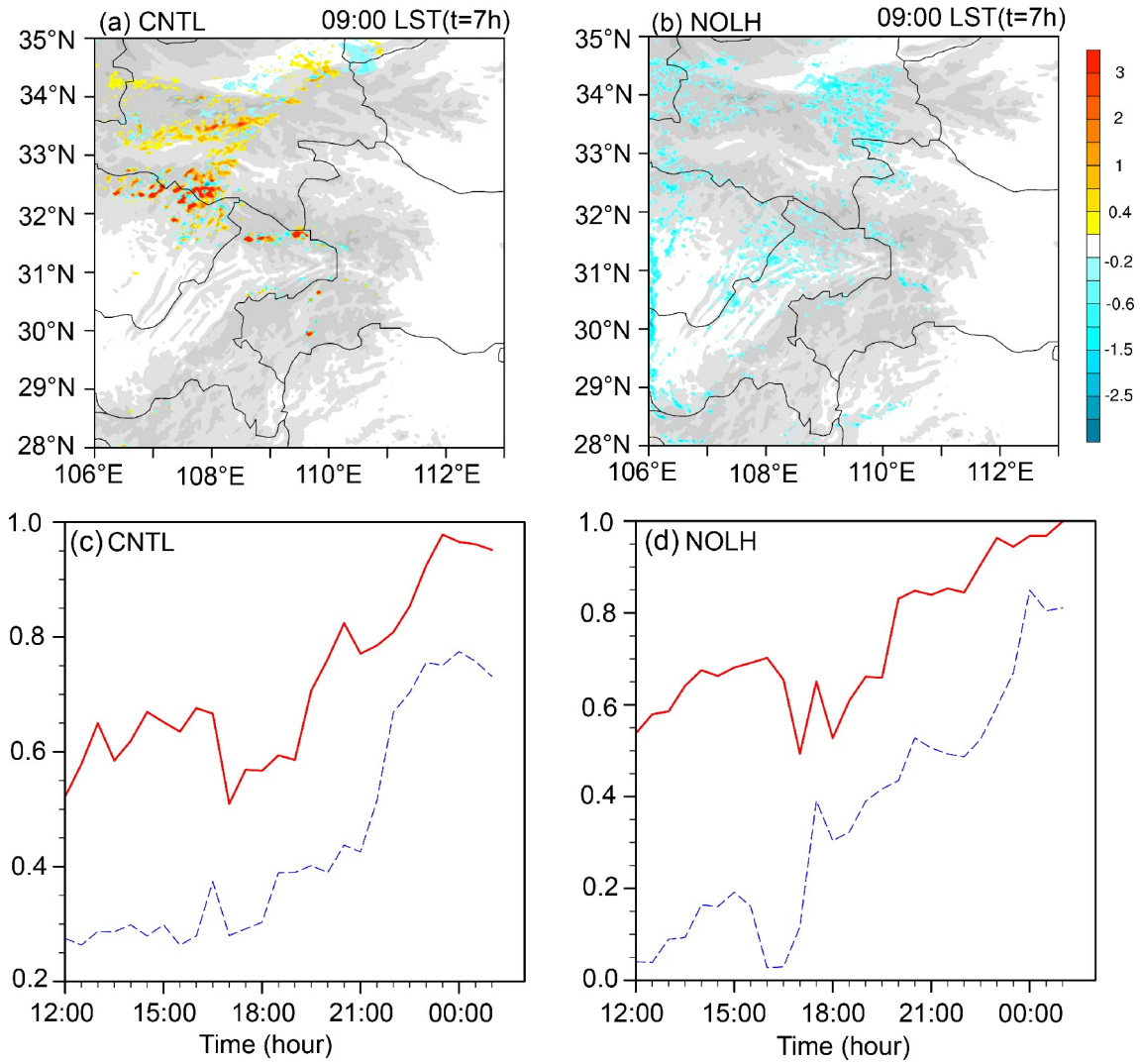


**Fig. 11.** Latent heating (units: $10^{-3}$ K $s^{-1}$) distribution at 700 hPa over the formation areas in CNTL (a) and NOLH (b). The grey shading represents terrain elevations > 500 m. Averaged vorticity over the key areas of the vortex at (c) 850 and (d) 925 hPa of CNTL (red lines) and NOLH (blue lines).

hPa is greater than that at 850 hPa (Figs. 11c, d). It means that the eastward-propagating MCS greatly impacted the development and maintenance of the downstream low-level vortex, especially at the 925 hPa level.

Throughout the simulation period of NOLH, heavy rainfall was generally lacking west of 114°E along the YHRV, except for the dispersed heavy rainfall distribution (Figs. 12a, b). This result implies that an eastward-propagating MCS directly influences the related precipitation in downstream regions. Additionally, because of the weak lower-level vortex east of the second-step terrain, the precipitation associated with the vortex also decreases. The MCV at 850 hPa matures at 2230 LST, causing heavy rainfall over YHRV (Fig. 12c). As for rainfall in the CNTL simulation, the rainbelt covers a larger area, and the accumulated precipitation is greater (Figs. 12c–e). In the later stages of the MCV, the precipitation in the two simulations mainly appears over the vortex center and its eastern section. Still, the rainfall in the sensitivity experiment is weaker and is less intense (Figs. 12d–f).

## 6. Conclusions and discussion

Based on the statistical analysis of eastward-propagating MCSs over the second-step terrain along YHRV (Yang et al., 2019, 2020), this study investigates the formation and development of a typical type of long-lived eastward-propagating MCS. We performed semi-idealized sensitivity testing using a numerical simulation from eight representative MCS cases. The conclusions are as follows.

First, eight eastward-propagating MCSs were selected based on similarities in their synoptic weather patterns and convection initiation conditions. Next, composite meteorological fields from the eight MCSs are used as initial and boundary conditions for WRF simulation. The semi-idealized simulation successfully reproduces the formation of convection over the second-step terrain, its eastward propagation, its merger with pre-existing convection in the downstream areas,

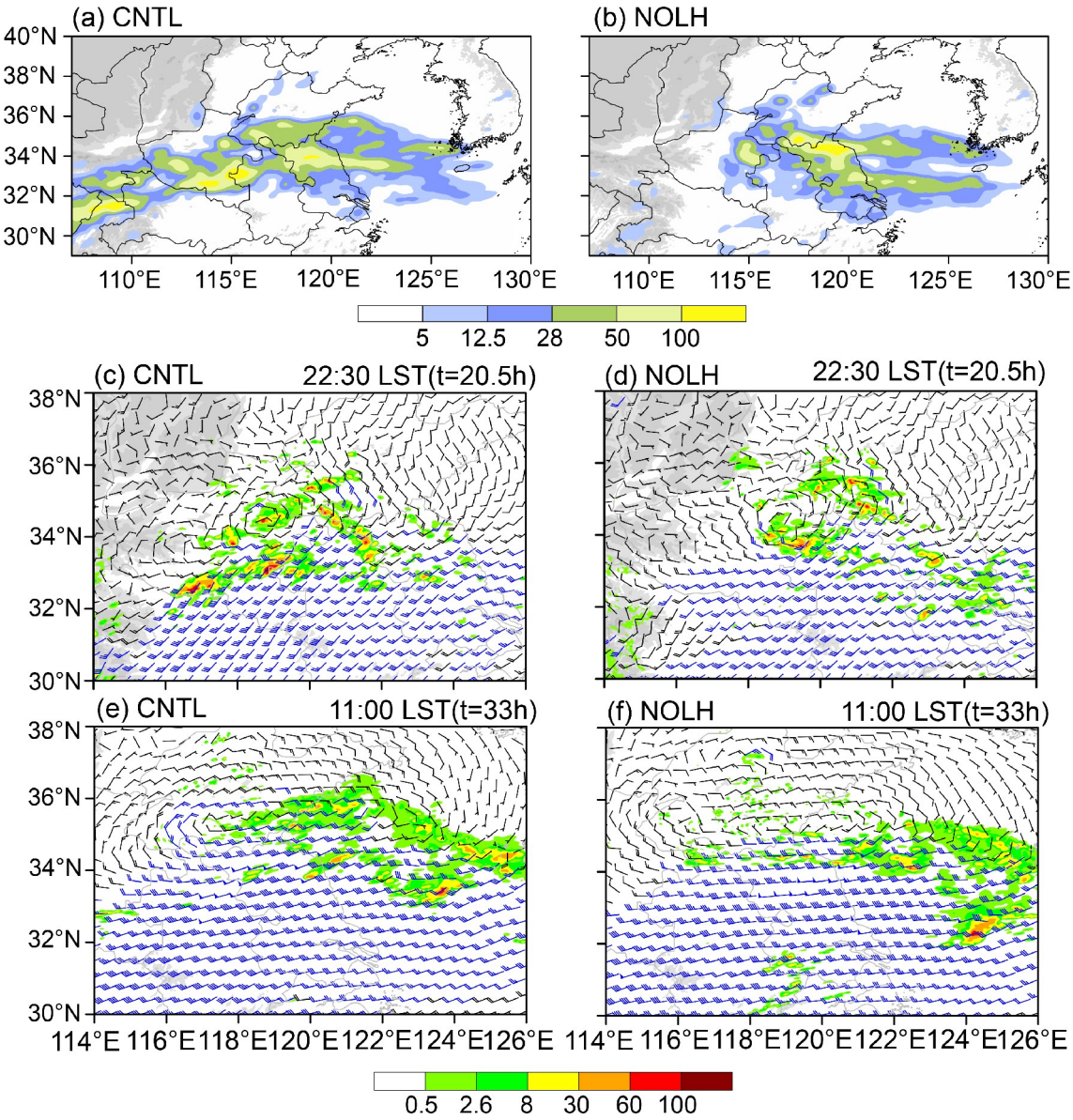


**Fig. 12.** Accumulated precipitation (units: mm) from the 11.5 to 36 simulation hours of CNTL (a) and NOLH (b). Wind field at 850 hPa (wind barb, 4 m $s^{-1}$; speeds with > 8 m $s^{-1}$ are indicated in blue) and precipitation (shading, units: mm $h^{-1}$) from the 20.5 and 33 simulation hours, (c) and (e) are for CNTL, (d) and (f) are for NOLH. The grey shadings represent terrain elevations > 500 m.

and the associated precipitation pattern. Results from the CNTL experiment indicate that the complete evolution of the MCS and its related MCV includes five stages: the MCS formation stage (1330–1530 LST), the propagation stage over the second-step terrain (1530–1900 LST), the MCV formation stage (1900–2300 LST), the maintenance stage (2300–0900 LST) and the dissipation stage (0900–1400 LST). Convection forms in regions with southwesterly winds in the low-to-midtroposphere commonly observed downstream of a 500 hPa shortwave trough. In this case, the shortwave was located east of the TP and on the northwest periphery of the WPSH, where abundant warm and moist air provides favorable moisture conditions for convection initiation. Convection initiation results from the release of CAPE triggered by the low-level convergence of southeasterly and northeasterly winds. After initiation, convection gradually propagates eastward under the influence of westerlies in the middle troposphere. During this time, moist convection develops and intensifies into MCS due to the low-level convergence and unstable stratification in the lower troposphere.

Figure 13 shows the conceptual model of the impact of an eastward-propagating MCS over the second-step terrain on the evolution of an MCV over downstream regions. While an MCS propagates out of the eastern edge of the second-step terrain and merges with the convection systems over the plains, the corresponding wind perturbation intensifies into a vortex at 850 hPa. The mesoscale vortex

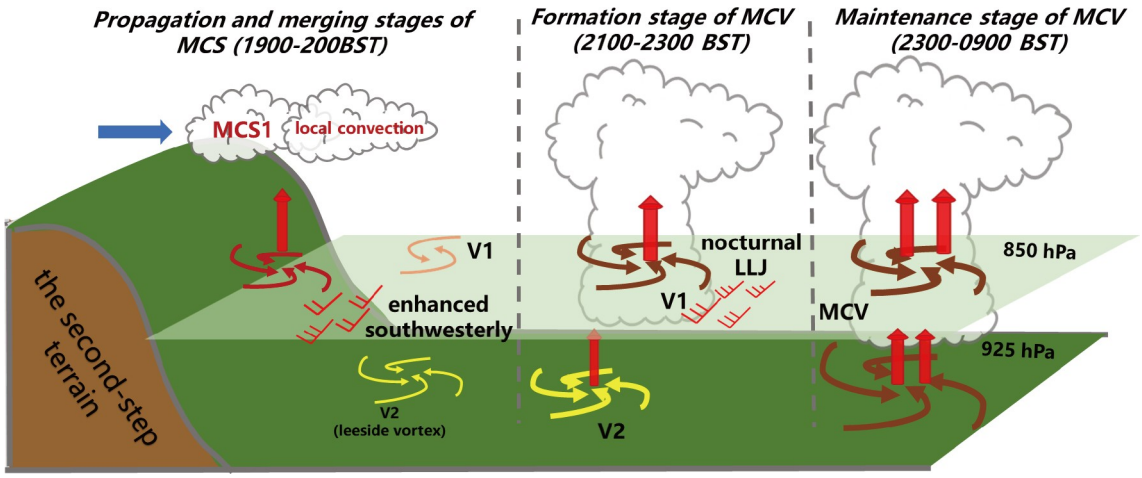


**Fig. 13.** The conceptual model of the impact of an eastward-propagating MCS over the second-step terrain on the evolution of MCV over the downstream regions, including stages: eastward-propagation of MCS1 out of the second-step terrain, merger with the local convection system, formation and maintenance of MCV.

moves eastward, and the enhanced southwesterlies on the southeastern periphery of this vortex gradually promote enough local wind convergence to develop a local vortex (V1) at 850 hPa. This intensified local vortex merges with the leeside vortex at 925 hPa (V2) and finally develops into a mature MCV. The presence of enhanced nocturnal LLJ enables the merged convection to develop further. The MCV then intensifies and moves eastward and subsequently merges with the continuously strengthening vorticity centers on its eastern (downstream) side. At this time, the MCV reaches the mature stage with notable precipitation along its southern flank where convergence associated with the LLJ is most strongly focused.

Results from the sensitivity experiment with diabatic heating in the formation region turned off indicate that MCSs do not form and move eastward over the second-step terrain when no diabatic heating is available. In the absence of eastward-propagating MCSs, convective and mesoscale vortices still exist in the plains to the east of the second-step terrain along YHRV, but the vortex strength and precipitation intensity weaken markedly. This result indicates that the eastward movement of these long-lived MCSs has a significant impact on the development and enhancement of convection and vortices in the downstream areas.

Based on a semi-idealized simulation from composite fields, the present study reveals the formation, development, and impact on downstream systems of a typical type of eastward-propagating MCSs. Future studies will analyze real cases and simulate them to gain a deeper understanding of the impact of second-step terrain along YHRV on the initiation of MCSs and the relevant mechanisms related to mesoscale vortices induced by eastward-propagating MCSs.

***Acknowledgements***. This article is dedicated to Prof. Fuqing ZHANG, who greatly contributed to our long-term international cooperation on mesoscale meteorology. We sincerely appreciate Prof. Fuqing ZHANG for all the suggestions, discussions, and help regarding the relationship between MCSs and mesoscale vortexes east of the second-step terrain in China. This research was supported by the National Key R&D Program of China (Grant No. 2018YFC1507200) and the National Natural Science Foundation of China (Grant No. 41975057).

## REFERENCES

Anderson, C. J., and R. W. Arritt, 1998: Mesoscale convective complexes and persistent elongated convective systems over the United States during 1992 and 1993. *Mon. Wea. Rev.*, **126**, 578–599, https://doi.org/10.1175/1520-0493(1998)126<0578:mccape>2.0.co;2.

Augustine, J. A., and K. W. Howard, 1991: Mesoscale convective complexes over the United States during 1986 and 1987. *Mon. Wea. Rev.*, **119**, 1575–1589, https://doi.org/10.1175/1520-0493(1991)119<1575:mccotu>2.0.co;2.

Augustine, J. A., and F. Caracena, 1994: Lower-tropospheric precursors to nocturnal MCS development over the central United States. *Wea. Forecasting*, **9**, 116–135, https://doi.org/10.1175/1520-0434(1994)009<0116:ltptnm>2.0.co;2.

Bai, A. J., X. D. Liu, and C. H. Liu, 2011: Contrast of diurnal variations of summer precipitation between the Tibetan Plateau and Sichuan Basin. *Plateau Meteorology*, **30**, 852–859. (in Chinese with English abstract)

Chen, F., and J. Dudhia, 2001: Coupling an advanced land surface-hydrology model with the Penn State-NCAR MM5 modeling system. *Part Ⅰ: Model implementation and sensitivity. Mon. Wea. Rev.*, **129**, 569–585, https://doi.org/10.1175/1520-0493(2001)129<0569:CAALSH>2.0.CO;2.

Chen, Q., J. W. Fan, S. Hagos, W. I. Gustafson Jr., and L. K. Berg, 2015: Roles of wind shear at different vertical levels: Cloud system organization and properties. *J. Geophys. Res.*, **120**, 6551–6574, https://doi.org/10.1002/2015JD023253.

Chen, X. C., F. Q. Zhang, and K. Zhao, 2016: Diurnal variations of the land-sea breeze and its related precipitation over South China. *J. Atmos. Sci.*, **73**, 4793–4815, https://doi.org/10.1175/JAS-D-16-0106.1.

Coniglio, M. C., D. J. Stensrud, and L. J. Wicker, 2006: Effects of upper-level shear on the structure and maintenance of

strong quasi-linear mesoscale convective systems. *J. Atmos. Sci.*, **63**, 1231–1252, https://doi.org/10.1175/jas3681.1.

Dudhia, J., 1989: Numerical study of convection observed during the winter monsoon experiment using a mesoscale two-dimensional model. *J. Atmos. Sci.*, **46**, 3077–3107, https://doi.org/10.1175/1520-0469(1989)046<3077:NSOCOD>2.0.CO;2.

Fu, S. M., J.-H. Sun, Y.-L. Luo, and Y.-C. Zhang, 2017: Formation of long-lived summertime mesoscale vortices over central East China: Semi-idealized simulations based on a 14-year vortex statistic. *J. Atmos. Sci.*, **74**, 3955–3979, https://doi.org/10.1175/jas-d-16-0328.1.

Fu, W., D.-H. Wang, H. Yin, J.-F. Yin, and J. Li, 2013: Constrct analysis on statistical characteristic of MCSs over Qinghai-Xizang Plateau and East Asia in warm season. *Plateau Meteorology*, **32**, 929–943, https://doi.org/10.7522/j.issn.1000-0534.2012.00089. (in Chinese with English abstract)

He, H. Z., and F. Q. Zhang, 2010: Diurnal variations of warm-season precipitation over northern China. *Mon. Wea. Rev.*, **138**, 1017–1025, https://doi.org/10.1175/2010mwr3356.1.

He, Z. W., Q. H. Zhang, K. Zhao, and H. Q. Hu, 2018: Initiation and evolution of elevated convection in a nocturnal squall line along the Meiyu front. *J. Geophys. Res.*, **123**, 7292–7310, https://doi.org/10.1029/2018JD028511.

Hong, S.-Y., and J.-O. J. Lim, 2006: The WRF single-moment 6-class microphysics scheme (WSM6). *Journal of the Korean Meteorological Society*, **42**, 129–151.

Hong, S.-Y., Y. Noh, and J. Dudhia, 2006: A new vertical diffusion package with an explicit treatment of entrainment processes. *Mon. Wea. Rev.*, **134**(9), 2318–2341, https://doi.org/10.1175/MWR3199.1.

Hu, L., D. F. Deng, S. T. Gao, and X. D. Xu, 2016: The seasonal variation of Tibetan convective systems: Satellite observation. *J. Geophys. Res.*, **121**, 5512–5525, https://doi.org/10.1002/2015jd024390.

Jiang, J. X., and M. Z. Fan, 2002: Convective clouds and mesoscale convective systems over the Tibetan Plateau in Summer. *Chinese Journal of Atmospheric Sciences*, **26**, 263–270, https://doi.org/10.3878/j.issn.1006-9895.2002.02.12. (in Chinese with English abstract)

Jirak, I. L., W. R. Cotton, and R. L. McAnelly, 2003: Satellite and radar survey of mesoscale convective system development. *Mon. Wea. Rev.*, **131**, 2428–2449, https://doi.org/10.1175/1520-0493(2003)131<2428:sarsom>2.0.co;2.

Kain, J. S., 2004: The Kain–Fritsch convective parameterization: An update. *J. Appl. Meteorol.*, **43**, 170–181, https://doi.org/10.1175/1520-0450(2004)04360;0170:tkcpau62;2.0.co;2.

Laing, A. G., and J. M. Fritsch, 1997: The global population of mesoscale convective complexes. *Quart. J. Roy. Meteor. Soc.*, **123**, 389–405, https://doi.org/10.1002/qj.49712353807.

Luo, Y. L., Y. Gong, and D.-L. Zhang, 2014: Initiation and organizational modes of an extreme-Rain-producing mesoscale convective system along a Mei-Yu front in East China. *Mon. Wea. Rev.*, **142**(1), 203–221, https://doi.org/10.1175/MWR-D-13-00111.1.

Maddox, R. A., 1980: Mesoscale convective complexes. *Bull. Amer. Meteorol. Soc.*, **61**, 1374–1387, https://doi.org/10.1175/1520-0477(1980)061<1374:MCC>2.0.CO;2.

Mathon, V., and H. Laurent., 2001: Life cycle of Sahelian mesoscale convective cloud systems. *Quart. J. Roy. Meteor. Soc.*, **127**, 377–406, https://doi.org/10.1002/qj.49712757208.

May, P. T, and A. Ballinger, 2007: The statistical characteristics of convective cells in a monsoon regime (Darwin, Northern Australia).. *Mon. Wea. Rev.*, **135**, 82–92.

Meng, Z. Y., D. C. Yan, and Y. J. Zhang, 2013: General features of squall lines in East China. *Mon. Wea. Rev.*, **141**, 1629–1647, https://doi.org/10.1175/mwr-d-12-00208.1.

Mlawer, E. J., S. J. Taubman, P. D. Brown, M. J. Iacono, and S. A. Clough, 1997: Radiative transfer for inhomogeneous atmospheres: RRTM, a validated correlated-k model for the longwave. *J. Geophys. Res.*, **102**, 16 663–16 682, https://doi.org/10.1029/97JD00237.

Qi, X. X., and Y. G. Zheng, 2009: Distribution and spatiotemporal variations of deep convection over China and its vicinity during the summer of 2007. *Journal of Applied Meteorological Science*, **20**, 286–294, https://doi.org/10.3969/j.issn.1001-7313.2009.03.004.

Rafati, S., and M. Karimi, 2017: Assessment of mesoscale convective systems using IR brightness temperature in the southwest of Iran. *Theor. Appl. Climatol.*, **129**, 539–549, https://doi.org/10.1007/s00704-016-1797-7.

Rasmussen, K. L., and R. A. Houze Jr., 2011: Orogenic convection in subtropical South America as seen by the TRMM satellite. *Mon. Wea. Rev.*, **139**, 2399–2420, https://doi.org/10.1175/mwr-d-10-05006.1.

Skamarock, W. C., and J. B. Klemp, 2008: A time-split nonhydrostatic atmospheric model for weather research and forecasting applications. *J. Comput. Phys.*, **227**(7), 3465–3485, https://doi.org/10.1016/j.jcp.2007.01.037.

Sun, J. H., and F. Q. Zhang, 2012: Impacts of mountain–plains solenoid on diurnal variations of rainfalls along the Mei-Yu front over the East China plains. *Mon. Wea. Rev.*, **140**, 379–397, https://doi.org/10.1175/mwr-d-11-00041.1.

Tollerud, E. I., and R. S. Collander, 1993: Mesoscale convective systems and extreme rainfall in the central United States. *Extreme Hydrological Events: Precipitation, Floods and Droughts,* Z. W. Kundzewicz et al., Eds., IAHS Publ. 213, 11–19.

Trier, S. B., and D. B. Parsons, 1993: Evolution of environmental conditions preceding the development of a nocturnal mesoscale convective complex. *Mon. Wea. Rev.*, **121**, 1078–1098, https://doi.org/10.1175/1520-0493(1993)121<1078:eoecpt>2.0.co;2.

Trier, S. B., C. A. Davis, and D. A. Ahijevych, 2010: Environmental controls on the simulated diurnal cycle of warm-season precipitation in the continental united States. *J. Atmos. Sci.*, **67**, 1066–1090, https://doi.org/10.1175/2009JAS3247.1.

Velasco, I., and J. M. Fritsch, 1987: Mesoscale convective complexes in the Americas. *J. Geophys. Res.*, **92**, 9591–9613, https://doi.org/10.1029/jd092id08p09591.

Yang, R., Y. Zhang, J. Sun, S. Fu, and J. Li, 2019: The characteristics and classification of eastward-propagating mesoscale convective systems generated over the second-step terrain in the Yangtze River Valley. *Atmos Sci Lett.*, **20**, e874, https://doi.org/10.1002/asl.874.

Yang, R. Y., Y. C. Zhang, J. H. Sun, and J. Li, 2020: The comparison of statistical features and synoptic circulations between the eastward-propagating and quasi-stationary MCSs during the warm season around the second-step terrain along the middle reaches of the Yangtze River. *Science China Earth Sciences*, **63**, 1209–1222, https://doi.org/10.1007/s11430-018-9385-3.

Yang, X. R., J. F. Fei, X. G. Huang, X. P. Cheng, L. M. V. Carvalho, and H. R. He, 2015: Characteristics of mesoscale convective systems over China and its vicinity using geostationary satellite FY2. *J. Climate*, **28**, 4890–4907, https://doi.org/10.1175/jcli-d-14-00491.1.

Zhang, Y. C., and J. H. Sun, 2017: Comparison of the diurnal variations of precipitation east of the Tibetan Plateau among sub-periods of Meiyu season. *Meteorol. Atmos. Phys.*, **129**, 539–554, https://doi.org/10.1007/s00703-016-0484-7.

Zhang, Y. C., J. H. Sun, and S. M. Fu, 2014: Impacts of diurnal variation of mountain-plain solenoid circulations on precipitation and vortices east of the Tibetan Plateau during the Mei-Yu season. *Adv. Atmos. Sci.*, **31**(1), 139–153, https://doi.org/10.1007/s00376-013-2052-0.

Zhang, Y. C., F. Q. Zhang, C. A. Davis, and J. H. Sun, 2018: Diurnal evolution and structure of long-lived mesoscale convective vortices along the Mei-Yu front over the East China plains. *J. Atmos. Sci.*, **75**(3), 1005–1025, https://doi.org/10.1175/jas-d-17-0197.1.

Zheng, L. L., and J. H. Sun, 2016: The impact of vertical wind shear on the intensity and organizational mode of mesoscale convective systems using numerical experiments. *Chinese Journal of Atmospheric Sciences*, **40**, 324–340, https://doi.org/10.3878/j.issn.1006-9895.1505.14311. (in Chinese with English abstract)

Zheng, L. L., J. H. Sun, X. L. Zhang, and C. H. Liu, 2013: Organizational Modes of Mesoscale convective systems over Central East China. *Wea. Forecasting*, **28**, 1081–1098, https://doi.org/10.1175/waf-d-12-00088.1.

Zheng, Y. G., J. Chen, and P. J. Zhu, 2008: Climatological distribution and diurnal variation of mesoscale convective systems over China and its vicinity during summer. *Chinese Science Bulletin*, **53**, 1574–1586, https://doi.org/10.1007/s11434-008-0116-9.

Zhuo, H., P. Zhao, C. H. Li, and Z. X. Pu, 2012: Analysis of climatic characteristics of mesoscale convective system over the lower reaches of the Yellow River during summer. *Chinese Journal of Atmospheric Sciences*, **36**, 1112–1122, https://doi.org/10.3878/j.issn.1006-9895.2011.11174. (in Chinese with English abstract)

Zipser, E. J., D. J. Cecil, C. T. Liu, S. W. Nesbitt, and D. P. Yorty, 2006: Where are the most intense thunderstorms on earth. *Bull. Amer. Meteor. Soc.*, **87**, 1057–1071, https://doi.org/10.1175/bams-87-8-1057.